Aerosol Effects on Electrification and Lightning Discharges in a Multicell Thunderstorm Simulated by the WRF-ELEC Model

Mengyu Sun[1,5], Dongxia Liu[1], Xiushu Qie[1], Edward R. Mansell[2], Yoav Yair[3], Alexandre O. Fierro[2,4], Shanfeng Yuan[1], Zhixiong Chen[1,5], Dongfang Wang[1]

5

[1] Key Laboratory of Middle Atmosphere and Global Environment Observation, Institute of Atmospheric Physics, Chinese Academy of Sciences, Beijing, China

[2] NOAA/National Severe Storms Laboratory, Norman, Oklahoma, USA

[3] Interdisciplinary Center (IDC) Herzliya, School of Sustainability, Herzliya, Israel

10   [4] Cooperative Institute for Mesoscale Meteorological Studies, University of Oklahoma, Norman, Oklahoma, USA

[5] College of Earth and Planetary Sciences, University of Chinese Academy of Sciences, Beijing, China

15   *Correspondence to*: Dongxia Liu (liudx@mail.iap.ac.cn)

Abstract

To investigate the effects of aerosol on lightning activity, the Weather Research and Forecasting (WRF) Model with a two-moment bulk microphysical scheme and bulk
20 lightning model was employed to simulate a multicell thunderstorm that occurred in the metropolitan Beijing area. The results suggest that under polluted condition lightning activity is significantly enhanced during the developing and mature stages. Electrification and lightning discharges within the thunderstorm show distinguish characteristics by different aerosol conditions through microphysical processes.
25 Elevated aerosol loading increases the cloud droplets numbers, the latent heat release, updraft and ice-phase particle number concentrations. More charges in the upper level

are carried by ice particles and enhance the electrification process. A larger mean-mass radius of graupel particles further increases non-inductive charging due to more effective collisions. In the continental case where aerosol concentrations are low, less latent heat releases in the upper parts and as a consequence, the updraft speed is weaker leading to smaller concentrations of ice particles, lower charging rates and less lightning discharges.

1 Introduction

Lightning activity is related to two important factors: dynamic-thermodynamic and microphysical characteristics (e.g. Williams et al., 2005; Guo et al., 2016; Wang et al., 2018; Zhao et al., 2020). Since the dynamic-thermodynamic processes affect the development of thunderstorm significantly, lightning activity is influenced by various dynamic-thermodynamic variables: temperature (Price, 1993), relative humidity in the lower and middle troposphere (Xiong et al., 2006; Fan et al., 2007), and convective available potential energy (Qie et al., 2004; Stolz et al., 2015), and many others.

The impacts of aerosol on the development of thunderstorm especially in metropolitan areas have been researched extensively. Observational studies indicated that the enhancement of lightning activity was related to increased cloud condensation nuclei (CCN) concentration (e.g., Westcott, 1995; Orville et al., 2001; Kar et al., 2009; Wang et al., 2011; Chaudhuri and Middey, 2013; Thornton et al., 2017; Yair, 2018; Qie et al., 2021). Kar et al. (2009) found a positive correlation between PM10 and SO_2 concentration and lightning flash densities around major cities in South Korea. A positive relationship between levels of particle pollution and lightning flash counts was also indicated by Chaudhuri and Middey (2013).

Furthermore, a variety of numerical simulations (e.g., Mitzeva et al., 2006) demonstrated the effects of aerosol on enhancing lightning activity. Using the Weather Research and Forecasting (WRF) Model with explicit spectral bin microphysics, Khain et al. (2010) found elevated aerosol increased the number of cloud droplets and the release of latent heat by acting as CCN. Therefore, more liquid water was lifted to

2

mixed-phase region by strong updrafts, with more ice-phase particles produced which can affect charge separation and lightning formation (Takahashi, 1978; Saunders and Peck, 1998; Takahashi et al., 1983; Mansell et al., 2005; Yair, 2008; Yair et al., 2021). Mansell and Ziegler (2013) suggested that greater CCN concentration led to greater lightning activity up to a point by testing a wide range of CCN concentration in a 3D model with two-moment bulk microphysics and stochastic branched discharge parameterization (Mansell et al., 2002). They also noted that average graupel density stayed high at lower CCN, but dropped at higher CCN because smaller droplets caused lower rime density. Zhao et al. (2015) showed that enhancing aerosol concentration resulted in an enhancement of electrification processes, due to the increasing growth rate of snow and graupel particles. However, Tan et al. (2017) simulated a thunderstorm in Changchun city with a 3D cumulus model coupled with aerosol module, electrification and lightning discharge, showing that the ice crystal and graupel number increased while the graupel mixing ratio decreased as the aerosol concentration increased.

The microphysical processes under different CCN concentration, especially the initiation and growth of ice-phase particles varied from different simulation studies. There are few studies that discussed the aerosol effects on thunderstorm with explicit electrification and discharge parameterization in the model simultaneously (e.g., Mitzeva et al., 2006; Mansell and Ziegler, 2013; Zhao et al., 2015). The detailed effects of aerosol on the discharging need further study.

By analyzing lightning data from the Beijing Lightning Network (BLNET) and PM$_{2.5}$ (particulate matter with aerodynamic diameter less than or equal to 2.5 μm) data, Sun et al. (2020) found a positive relationship between flash counts and PM$_{2.5}$ concentration prior to the occurrence of thunderstorm. As a mega city, Beijing has higher aerosol concentration resulting from anthropogenic air pollution. Still, the effects of aerosol on both electrification and discharges have been rarely discussed in this area by numerical simulation. Therefore, in this paper we present sensitivity studies on how the different CCN concentration influence the characteristic of thundercloud over the metropolitan Beijing area using the WRF-ELEC (Fierro et al., 2013). We conducted

3

sensitivity studies to evaluate the response of the microphysical properties, as well as electrification and lightning processes to aerosol characteristics. This paper is organized as follows: section 2 describes the data and methodology used in the study, section 3 introduces the design of simulations, section 4 presents the results, and section 5 discusses and summarizes the study.

2 Data sources

2.1 Observational dataset

Total flash numbers were obtained from the Beijing Lightning Network (BLNET), which consists of 16 stations covering East-West 110 km and North-South 120 km areas since 2015 (refer to Figure 1). The BLNET provides 3D-location results of flashes, including both intra-cloud (IC) and cloud-to-ground (CG) lightning (Wang et al., 2016). The average detection efficiency of the BLNET is 93.2% for the total flashes (Srivastava et al., 2017). In this study, the 3D-location lightning radiation pulses were grouped in flashes based on the criteria of 400 ms and 15 km. This grouping criteria was modified from the algorithm in Srivastava et al. (2017). In section 3, the lightning frequency from BLNET was calculated in every 6 min intervals, corresponding to the time span of Doppler radar scanning. In addition, the radar reflectivity data was obtained from an S-band Doppler radar (Chinese CINRAD/SA) near Beijing urban area (39.81 °N, 116.47 °E), and were updated every 6 min. The vertical levels vary from 500 m to 20 km and were processed into composite radar reflectivity with a horizontal resolution ($0.01 °\times0.01 °$). The precipitation data are taken from 295 gauge stations in a weather monitoring network of automatic weather stations in the Beijing region (refer to Figure 1), with spacing of approximately 3 km in urban area. The real-time hourly average ground levels of $PM_{2.5}$ are from the China National Environmental Monitoring Center (http://106.37.208.233:20035/ accessed on 2 May 2021).

2.2 Synoptic background

A mesoscale convective system over the Beijing area influenced by a strong Mongolia cold vortex on 11 Aug 2017 was simulated in this study. Based on the weather map at 00:00 UTC (figure not shown), there was a prevailing westward airflow in the south of the cold vortex, which brought dry cold air in middle layer. At low-level of 850 hPa, the southwesterly jet transported warm and humid air mass, forming an unstable condition together with cold air mass above. The sounding profile over Beijing (39.9 °N, 116.2 °E) exhibited an unstable thermodynamic condition for thunderstorm initialization, as shown in Figure 2, with a surface-based convective available potential energy (CAPE) of 3937 J kg^{-1} at 12:00 UTC. The special terrain condition with mountain in the northwest and ocean in the southeast (Qie et al., 2020), as well as heat island effect and elevated aerosol loading in the urban region (Zhang et al., 2013; Liu et al., 2018), likely enhanced the convection and were responsible for the occurrence of heavy rainfall and large hail as well as intensive lightning activity in the Beijing area. According to the surface-based automatic weather observation network in Beijing, the average rainfall in the urban area and the eastern region was 10-30 mm, with locally exceeding 100 mm. The total lightning flashes of this case accounted for one-third of the total number of lightning flashes during the 2017 warm season (Chen et al., 2020).

3. Model overview

The WRF Model (version 3.9.1) coupled with bulk lightning model (BLM, Fierro et al., 2013) and a two-moment bulk microphysics scheme (Mansell et al., 2010; Mansell and Ziegler, 2013) was used to simulate the multicell thunderstorm that occurred on 11 August 2017 in the Beijing metropolitan area.

The simulations employ the two-moment bulk microphysics scheme of Mansell et al. (2010), which predicts both mass mixing ratio and number concentration for a range of hydrometeor species (droplets, rain, ice crystals, snow, graupel, and hail). Microphysical processes include cloud droplet nucleation, condensation, collection-

coalescence, riming, ice multiplication, freezing and melting, and conversion between different hydrometeors, etc. It is noted that the predicted graupel density is variable, which makes it possible for the single graupel category to represent a range of particles from high-density frozen drops to low-density graupel (Mansell et al., 2010). The graupel growth processes contain collection of ice crystals by graupel, collection of snow particles by graupel, deposition of vapor to graupel, collection of supercooled water (cloud droplets and/or raindrops) by graupel, and conversions between hydrometeors. Further details of the interactions among particles can be found in Mansell and Ziegler (2013), Mansell et al. (2010), and Ziegler (1985). The CCN concentration is predicted as a bulk activation spectrum and initially mixed well vertically, following Eq. (1) of Mansell et al. (2010):

$$N_{CCN} = CCN \times S^k, \tag{1}$$

where CCN is the assumed CCN concentration, S is the supersaturation with respect to liquid water, and $k = 0.6$. The initiation of cloud droplets (both for cloud base and in-cloud) is based on Twomey (1959) and adjusted by Mansell et al. (2010).

Explicit charging physics includes both non-inductive charging (Saunders and Peck, 1998) and inductive or polarization charging (Ziegler et al., 1991). We employed non-inductive electrification scheme described by Saunders and Peck (1998) and adjusted by Mansell et al. (2005) in this study. The magnitude of charge separated within a grid cell (δq) is calculated from the non-inductive critical charging curve as a function of temperature and riming accretion rate (RAR), following Eq. (2) of Mansell et al. (2005):

$$\delta q = B D_{n,1}^a \left(\overline{V}_g - \overline{V}_I \right)^b q_\pm(RAR), \tag{2}$$

where B, a, b are a function of crystal size; $D_{n,1}^a$ is the mean volume diameter of the ice crystal-snow, $\overline{V}_g$ and $\overline{V}_I$ are the mass-weighted mean terminal fall speeds for graupel and ice crystal; the $q_\pm(RAR)$ is the charge separation as a function of the RAR from Brook et al. (1997) adjusted by Mansell et al. (2005). Non-inductive (i.e., independent of external electric fields) charge separation resulting from rebounding collisions between various ice-phase particles (ice, graupel, snow, hail) are all

6

parameterized based on results obtained from laboratory experiments (Takahashi, 1978; Saunders et al., 2001; Mansell et al., 2005). Inductive charging requires a pre-existing electric field to induce charge on the surfaces of the colliding particles (Mansell et al., 2005). Numerical experiments (Mansell et al., 2010) found that total inductive charging, is about an order of magnitude weaker than non-inductive charging, but can be important for lower charge regions. Only collisions between cloud droplets and ice-phase particles (graupel, ice, hail) are considered for inductive electrification. The electric field is simulated by solving Poisson equation for the electric potential Φ:

$$\nabla^2 \Phi = -\frac{\rho_{tot}}{\varepsilon}, \tag{3}$$

where ρ_{tot} is the net space charge and ε is the electric permittivity of air (8.8592×10^{-12} F/m). A message-passing-interface (MPI) black box multigrid iterative solver or BoxMG algorithm (Dendy, 1987) is extended to solved Eq. (3). And then the three components of the electric field and its magnitude are computed from Eq. (4):

$$E = -\nabla \Phi, \tag{4}$$

The discharge model parameterization from Ziegler and MacGorman (1994) is used within a cylindrical region (Fierro et al., 2013). A flash would be initiated when the electric field exceeds a breakdown threshold, which variants of vertical electric profile of Dwyer (2003) at a model grid point (from here on, we shall use the term 'grid points' for short). A discharge is centered at the initiation grid points within a cylinder of extending vertically through the depth of the domain. If the space charge magnitude at a grid point exceeds a specific space charge threshold (0.1 nC m^{-3} herein), this grid point will be involved in discharge within the cylinder during this time step. After each discharge, the charge magnitude is set to 70% (Rawlins, 1982; Ziegler and MacGorman, 1994) of the summed magnitude for all grid points. Then the charges will be redistributed throughout all discharge volumes and the electric field is be recalculated. The discharge in each time step will be terminated until the maximum electric field no longer exceeds the breakdown threshold. An estimate of flash origin density (*FOD*) rate (over a time period $T = t_2 - t_1$) is computed following Eq. (5):

$$FOD(T) = \frac{G}{C} \int_{t_1}^{t_2} B(t)dt, \tag{5}$$

where G is the horizontal grid cell area, C the cylinder cross sectional area (set in the

200　following simulations to radius R = 12 km (Fierro et al., 2013)). In this study, the

integral represents the sum of flashes $[B(t)]$ that extend into the grid column for all the

time steps within the time period *T*. Further, flash extent density (*FED*) are given by

Eq. (6). Thus, the predicted flash extent density over the Beijing area in section 3 is the

FED calculated in 6 min intervals:

205　$FED(T) = \sum FOD(T).$ 　　　　　　　　　　　　　　　　　(6)

3.1 Design of the simulations

The nested model configuration for the simulations are shown in Table 1. The

WRF-ELEC model is configured by a two-way interactive nested domain. The outer

210　domain has a horizontal grid spacing of 6 km (442×391 grid points) and the inner

domain is 2 km (496×496 grid points), both centering at (40 °N, 116.05 °E). The number

of vertical levels are 40 and the top is set to 50 hPa for the two domains. The model

physics configuration is the Unified Noah Land Surface Model (Chen and Dudhia,

2001). The longwave and shortwave radiation are parameterized following the Rapid

215　Radiation Transfer Model (Mlawer et al., 1997) and the Dudhia scheme (Dudhia, 1989),

respectively. The Bougeault-Lacarrere PBL scheme is used to parameterize the

boundary layer processes (Bougeault and Lacarrere, 1989). Simulations began at 00:00

UTC on 11 August 2017 and integrated for 24 h. The period of interest was from 09:00

UTC until 17:00 UTC (time in the simulations). The 3-hourly NCEP GFS (Global

220　Forecast System) data with 0.5 °×0.5 ° resolution are used to establish the initial and

boundary conditions.

To survey the aerosol effects on the structure of thunderstorm and lightning

activity, two sensitivity experiments are performed with different CCN concentration:

a polluted case (P-case) and a continental case (C-case). Figure 3 shows hourly average

225　mass concentration of $PM_{2.5}$ on 11 August 2017. The hourly-average value of the

observed $PM_{2.5}$ concentration before the thunderstorm initiation (more than 110 μg m⁻

[3]) is much higher than the 3-year mean $PM_{2.5}$ concentration (69.4 ± 54.8 µg m^{-3}) in the Beijing area (Liu et al., 2018). Therefore, the CCN concentration is selected as the P-case which is consistent with observation. The initial value for the P-case is set as a number mixing ratio relative to sea level air density ρ_0: $2000/\rho_0\times10^{-6}$ kg^{-1}, where $\rho_0=1.225$ kg m^{-3}, and the local number concentration is $2000\times(\rho_{air}/\rho_0)$ cm^{-3}. And the initial number concentration for the C-case is set at $1200\times(\rho_{air}/\rho_0)$ cm^{-3}, consistent with typical continental conditions (e.g. Hobbs and Rangno, 1985; Mansell et al., 2005; Mansell, personal communication, 2019). The relatively high prescribed CCN concentration guaranteed small droplet diameters and should be effectively delayed the warm rain process in the model (Mansell and Ziegler, 2013).

4 Results

4.1 Radar reflectivity, precipitation and lightning flashes of multicell

Figure 4 shows the observed and simulated radar reflectivity at different periods for both cases, with the formation of thunderstorms in the simulation earlier than the observation about 1.5 h. For this reason, we display the simulation and observation with ~90 minutes time difference. It is clear that both simulated times in the P-case exhibit an overall good agreement with the evolution and morphology of the radar echo, especially evidenced by the northeast-southwest orientation of the radar echo at 11:54 UTC in the simulated polluted case (13:24 UTC in the observation). We also present the comparison of radar reflectivity as a function of height from the observation and simulations in the corresponding periods (Figure 5). According to the morphology and intensity of the radar echo, the observed radar reflectivity is in better agreement with simulated radar reflectivity only in the polluted case. Note that the modeled reflectivity differs from the observation in the northwestern area (115.4 °E-116.0 °E, Fig. 4a, 4c and 4e), the impacts of aerosol on lightning activity will only be evaluated in the southeastern Beijing area (39.4 °N-40.6 °N, 116.0 °E-117.5 °E, shown in Fig. 4d; here on, 'domain' for short).

255   Precipitation measurements from around 300 gauge stations in the Beijing area are compared with the WRF simulations. Figure 6 shows hourly peak rainfall rate from the rain gauges and from simulations for the P-case and C-case. As noted, the formation of thunderstorm in the simulations occurring about 1.5 h earlier than in the observation. So we display the simulations and observation with a 1 h time shift. It can be seen that

260   the peak rainfall rate reaches the maximum at the same stage of development in both simulations (at 12:00 UTC) and the measurement (at 13:00 UTC). The rainfall in the P-case continues for around 9 hours, which is consistent with the gauge measurement, while the rainfall in the C-case lasts one hour less than the observation. The maximal peak rainfall rate in the P-case is 97.3 mm/h, which is larger than the measurement (and

265   the C-case) with a value of 80 mm/h (77.3 mm/h). The difference in the rainfall rate is further analyzed through the comparison of spatial distribution of precipitation. Figure 7 displays the 6-hourly accumulated precipitation from the observation (11:00-17:00 UTC) and from the simulations for the P- and C-case (10:00-16:00 UTC). Both the simulations reproduce the precipitation in the southeastern region, where the gauge

270   measurements show the accumulated rainfall are exceeding 100 mm. The coverage of the simulated precipitation in the P-case extends to the northeast area compared to the C-case, which is more consistent with the observation. This area is included in our analyzed region shown in Figure 4d.

    The temporal variation of total flashes from BLNET is shown in Figure 8a,

275   including both intra-cloud (IC) and cloud-to-ground (CG) lightning. The lightning frequency gradually increased during 11:00-12:00 UTC and raised significantly after 12:00 UTC, as well as reached the peak value at 12:30 UTC, and then decreased gradually. According to the evolution of radar reflectivity and lightning activity (Van Den Broeke et al., 2008; Kumjian et al., 2010, Liu et al., 2021), the real and simulated

280   developments of the thunderstorm are shown in Table 2. The temporal evolution of predicted FED over Beijing area under the polluted and continental cases are shown in Fig. 8b, both of them start earlier than observation about 1.5 h. Compared to the continental case, the variation of predicted flashes under polluted condition is better consistent with the observation. The predicted FED for the P-case and measured flashes

increase significantly after 10:00 UTC (11:30 UTC in the observation), and reach the peak around 11:00 UTC (12:30 UTC in the observation). In contrast, the predicted flashes for the C-case reaches the peak around 10:30 UTC, earlier than the P-case and measured lightning flashes, and then decreases dramatically. Within the duration of the thunderstorm, the overall FED in the polluted case is noticeably about 50% higher than the C-case.

Figure 9 displays the number of initiations over the Beijing area for the C-case and P-case during different periods. To examine the details of lightning response to aerosol, the intensity of lightning activity can be categorized into four levels by the lightning grid points in each time step: light (50-100 grid points), moderate (100-200 grid points), heavy (200-300 grid points) and extreme (>300 grid points). Then the number of points (grid columns) in each category is counted hourly as the 'number of initiations'. A comparison of the different lightning intensity categories reveals that the simulated lightning activities increase during 10:30-12:30 UTC (Fig. 9b and 9c) under high aerosol loading, corresponding to the developing and mature stages of the thunderstorm. During 09:30-10:30 UTC, while different categories of lightning intensity are enhanced for both P- and C-case (Fig. 9a), it is noted that the maximum lightning initiation occurs in the extreme level for the P-case. In the dissipating stage, lightning activities decrease dramatically in the P- and C-case (Fig. 9d), but the lightning intensity under polluted condition is still stronger compared to the C-case. Hence, the results indicate that elevated aerosol loading enhances lightning activities especially in the developing and mature stages of thunderstorm. In the following contents we will offer a possible explanation for this effect.

4.2 Microphysical properties of multicell

To investigate the effects of aerosol on lightning activities, we first analyze the simulated microphysical properties in both the continental and polluted sensitivity studies. Figure 10a-10h show the temporal variations of the vertical profiles for

different hydrometeors. For each quantity, the mass mixing ratio and number concentration of hydrometeors are averaged horizontally over the analyzed region at a given altitude. The domain-averaged microphysical properties for the various hydrometeors are summarized in Table 3. The domain-average mean-mass $radius_h$ of hydrometeors in Table is calculated following Eq. (7):

$$radius_h = [\frac{1}{c_h} \times \frac{Sum(\rho_{air}(i,j,k) \times q_h(i,j,k))}{Sum(\rho_{air}(i,j,k) \times n_h(i,j,k))}]^{1/3}, \tag{7}$$

where ρ_{air} is the air density, and c_h, q_h, n_h are the density, mass concentration, and number concentration of hydrometeor species h (Mansell et al., 2010), respectively. Figure 10i-10j display the time-height plots of maximum radar reflectivity and vertical velocities. The related convective properties are shown in Table 4.

It can be seen that elevated aerosol loading results in increasing cloud droplet concentrations (Figure 10b and Table 3). Under polluted condition, more aerosols could be activated into cloud droplets and more water vapor condenses onto these droplets, leading to large cloud water content and small droplet size (Lynn et al., 2007; Wang et al., 2011; Zhao et al., 2015; Jiang et al., 2017). Thereby, relatively more latent heat of condensation released in the P-case where large cloud water content exists, which can be seen in the vertical distribution of peak latent heat (Figure 12). The temporal variation of domain-averaged mean-mass radius for cloud droplets is shown in Figure 11. Under polluted condition, cloud droplets with smaller mean-mass radius are too small to be converted into raindrops. As a consequence, the rainwater mass mixing ratio is less in the polluted case compared to the continental one (Figure 10d). Instead, these cloud droplets could be transported to higher levels (< -40 ℃) by the strong updrafts resulting from increased latent heat. Previous studies showed that larger vertical velocities were driven by increased microphysical latent heating. (Wang et al., 2011; Mansell and Ziegler, 2013; Altaratz et al., 2017; Fan et al., 2018; Li et al., 2019). As shown in Table 4, the maximum updraft in the P-case (53.5 m/s) occurs above 12 km, while the height of maximum velocity for the C-case (50.4 m/s) is 10.5 km. As a result, the mixed-phase processes are enhanced and there are more ice crystals in the P-case above 10 km (Figure 10h). Observations and simulations also found that the content of

ice crystals could be greater under polluted condition, resulting from more condensation latent heat and strengthened updrafts (Khain et al., 2008; Koren et al., 2010; Wang et al., 2011; Zhao et al., 2015; Tan et al., 2017; Lynn et al., 2020). The number concentration of ice crystals is much larger under polluted condition (Table 3), with domain-average of 3850×10^3 kg^{-1} for the polluted case and 2280×10^3 kg^{-1} for the continental case. The size of raindrops in the P-case is larger, which is also be found in Wang et al. (2011), probably due to the melting of ice-phase particles. These differences between cloud, rain droplets and ice crystals are directly influenced by the increasing aerosol loading. It is worth noting that the maximum of peak latent heat in the P-case occurs above 10 km at 09:30 UTC (Figure 12), indicating that more cloud droplets are lifted to the upper levels (< -40 ℃) and converted into ice crystals at the beginning stage of the thunderstorm. As noted, the latent heat shown in Figure 12 results from both condensation and freezing. The high value of latent heat existed in the higher levels (above 10 km) reveals a large amount release of frozen latent heat. Previous studies also found that elevated aerosol loading contributed to the increasing of frozen latent heat (e.g., Khain et al., 2005; Lynn et al. 2007; Storer et al., 2010; Li et al., 2017). The increased frozen latent heat during this period, together with relatively enhanced condensation latent heat, further ensure vigorous vertical growth and lead to the maximum updraft occurred at 10:48 UTC in the P-case.

In contrast, the domain-averaged mass mixing ratio of graupel is relatively less in the P-case (Figure 10e and 10f). Less graupel content under polluted condition is rather surprising, since previous simulation studies (Wang et al., 2011; Zhao et al., 2015) found that there could be more graupel at the mature stage of thunderstorm, by virtue of enhanced convection and more cloud droplets lifted to the mixed-phase region. These could happen if starting from a much lower CCN concentration (< 400 cm^{-3}), in this study, with higher CCN concentration (> 1000 cm^{-3}), the reduced raindrop freezing (Fig. 10d) probably explains the lower density of graupel. Smaller fall speed of the lower density graupel further lead to less riming and graupel contents. Other simulation also found a decrease of graupel mixing ratio under polluted conditions, and partly attributed the decrease to the melting of graupel particles (Tan et al., 2017). In this study, the

13

graupel content was higher in the C-case, probably owing to higher rainwater content and corresponding raindrop freezing. It is worth noting that the number concentration of graupel in the polluted case is rather less compared to the continental one (Table 3), with 12 kg^{-1} for the P-case, and 28 kg^{-1} for the C-case, respectively. Such a phenomenon could offer a partial explanation for the graupel of larger mean-mass radius appearing in the P-case (Figure 11c and Table 3). The domain-averaged mean-mass radius of graupel reaches 479.5 μm for the P-case, compared to 322.4 μm for the C-case. In contrast to the small difference in mean-mass radius of ice crystals between the polluted and continental cases (Figure 11d), the radius of graupel is much larger in the P-case. This likely results in a larger collision efficiency between graupel and other ice-phase particles, enhancing non-inductive charging.

Increasing aerosol loading affects the key microphysical processes, especially in the ice-phase processes yielding to larger ice crystal content/mass and larger graupel size. Both of them would inevitably affect lightning activity by affecting the rate and magnitude of charge separated during ice-graupel collisions.

4.3 The relationship between electrification, microphysics and dynamics

The time series of the peak positive (negative) charge density in the two cases are shown in Figure 13. The domain-averaged peak charge structure in the P-case is similar to that of the C-case before 12:00 UTC, with positive charge region distributed above the negative charge region. In both cases, the maximum peak positive charge density occurs above 8.5 km (< -30 ℃). While the peak charge density for the polluted case is significantly greater, especially at the developing and mature stages (10:00-12:00 UTC). The peak positive charge density for the P-case is more than +4 nC m^{-3} during this period, but the peak charge density is less than +2 nC m^{-3} in the C-case. With the development of the thunderstorm, the charge density decreases gradually for both cases. At the upper levels, the peak charge density is still greater and lasts longer under polluted condition.

400   To analyze the relationship between hydrometeors and electrification, vertical cross sections are shown in Figure 14a and 15a, which display the total charge distribution at the mature stage of the thunderstorm in the polluted (11:54 UTC) and continental cases (11:24 UTC), respectively. It is noted that the vertical profiles of the charge distribution are more detailed than the domain-averaged charge structure shown

405   in Figure 13. The charge structure with positive charge in the upper levels and negative charge in the lower levels was simulated in the C-case. There were positive charge appeared in the lower negative charge center (Fig. 15a), which means that this charge structure is a little different from the normal dipole (upper charge positive, lower charge negative; e.g., Thomas et al., 2001). While the positive charge magnitude in the lower

410   levels for the C-case is relatively small to form normal tripole, in which a dominant region of negative charge with positive charge above and a positive charge below with approximately the same order of magnitude of charge (Simpson and Scrase, 1937; William et al., 1989). In the polluted case, with a negative charge region in the upper level (above 13 km), the updraft region exhibited an charge structure with a positive

415   charge center located in the middle, and two negative charge centers in the upper and lower levels; e.g. Mansell et al., 2005). For the total net space charge density, the maximum of positive charge density at the mature stage in the P-case is up to +1 nC m^{-3}, which is much higher than that in the C-case (less than +0.5 nC m^{-3}).

        We attempt to explain the origins of the charge distribution by examining the

420   polarity and amount of charge carried by different hydrometeor species (namely by ice, graupel, snow and hail particles). The negative charge region in the upper levels (12-15 km) for the P-case resulted from collisions of graupel particles with smaller ice crystals and snow particles (Fig. 14d), with the 30 dBZ echo tops reaching 13 km. The simulated vertical distribution of net charge in the C-case was caused by ice and snow particles

425   charged positively at 8-12 km and graupel particles charged negatively at 4-7 km, respectively (Fig. 15b and 15d). The collisions between graupel and hail particles could partially explain the intense positive charge center located at 8-12 km in the P-case. Less ice-phase particles appear in upper level in the continental case compared to the polluted one, corresponding to a relatively weaker charge center. Figure 14c and 15c

430   show the cross sections of the simulated radar reflectivity and vertical velocity at 11:54

UTC (11:24 UTC) under different aerosol conditions. It is evident that both updraft and

downdraft for the polluted case are greater than that for the continental one at higher

levels, resulting from more frozen latent heat, and as a consequence, the total charge

density is significantly greater above 12 km.

435   According to Saunders and Peck (1998) non-inductive charging curve, graupel

charged negatively within regions of relatively weak updrafts (< 5 m s^{-1}) and lower

liquid water content (LWC), forming a negative charge region at 4-8 km in the P-case

(Fig. 14a and 14d). With higher LWC in the polluted case, graupel, ice and hail were

charged positively, forming a strong positive charge center at 9km (< -20 ℃), as shown

440   in Fig. 14a. The simulations show that non-inductive charging mechanism plays a main

role at the mature stage, the rate of which is one order of magnitude larger than inductive

charging (Fig. 16). As described in section 4.2, more ice particles and graupel with

larger radius appeared at this stage in the P-case, evidenced by the larger simulated

radar reflectivity (Fig. 14c), and the ensuing collision rates led to significantly stronger

445   non-inductive charging at 6-10 km (Fig. 16b). In consequence, it is obvious in the

Figure 14a and 15a that the charge density for the P-case is much higher than the C-

case, indicating that aerosol plays an important role in affecting the accumulated charge

density through microphysical and further electrical processes.

The appearance of more ice-phase particles in upper level, increasing ice crystal

450   number and mean-mass radius of graupel particles, together led to greater charge

densities and as a consequence to stronger electric field intensities. Lightning discharge

in the WRF-ELEC occurs if the electric field magnitude exceeds a prescribed, fixed

threshold, which further supports the important role of aerosols in enhancing storm

electrification. Mansell et al. (2013) found that greater CCN concentration led to

455   increased lightning activity up to a point, by affecting microphysical and electrical

characteristics, with a large sensitivity to ice multiplication. In agreement with Mansell

et al. (2013), this study showed that higher CCN concentration in the polluted case

resulted in a relatively strong upper charge region, together with increased charge

density and electric field intensity, finally enhancing lightning activity, as shown in

460   Figure 8b.

5 Conclusions and discussion

To elucidate the effects of aerosol on lightning activity, a two-moment bulk microphysics scheme (Mansell et al., 2010; Mansell and Ziegler, 2013) and bulk

465   lightning model (BLM, Fierro et al., 2013) were coupled in the WRF model to simulate a multicell thunderstorm that occurred on 11 August 2017 in the metropolitan Beijing area. The simulated distributions and spatio-temporal development of radar reflectivity and precipitation under polluted condition are in overall agreement with observations.

Sensitivity experiments show that the intensity and duration of lightning activity

470   are evidently different between moderate (continental) and high (polluted) aerosol concentrations, resulting from microphysical processes. Elevated aerosol concentrations lead to increasing cloud droplet contents and smaller droplet size. Smaller droplets suppress collection/coalescence processes and lead to the less rainwater under polluted condition. These cloud droplets which could not accreted by

475   raindrops will be transported to higher levels and convert into ice crystals. Increased latent heat release leads to strong updrafts, and in turn more cloud droplets could be lifted up. As a result, the ice crystal contents are much greater in the P-case. Although the graupel contents are relatively less under polluted condition resulting from less raindrop freezing, the radius of graupel is much larger in the P-case due to much less

480   number concentration. Consequently, elevated aerosol loading enhances the development of ice-phase microphysical processes, evidenced by more ice crystals and larger radius of graupel participating in charge-separation and electrification processes. Non-inductive charging increases due to more frequent and effective collisions between graupel and other ice-phase particles. These bring about higher charge density, together

485   with larger upper charge region caused by more ice-phase particles lifted to higher levels, leading to electric field magnitudes which exceed the breakdown threshold value, eventually culminating in an enhanced lightning activity. During the developing and mature stages of the thunderstorm, the latent heat release at higher altitude is noticeably

17

greater in the P-case, mainly due to the release of frozen latent heat from supercooled
liquid particles.

Observation and simulation studies found that elevated aerosol loading enhanced the electrical activity (e.g., Koren et al., 2010; Wang et al., 2011). Some previous studies suggested that the mass mixing ratio of ice and graupel increased with the enhanced CCN concentration, eventually resulting in stronger lightning activity (e.g., Wang et al., 2011; Zhao et al., 2015), while a decrease of graupel mixing ratio was found by Tan et al. (2017). It should also be noted that when aerosol concentrations are too large, this leads to the inhibition of convection resulting in less lightning, as discovered by Altaratz et al. (2010) in the Amazon basin, as well as by Hu et al. (2019) in Houston region, and simulated by Mansell and Ziegler (2013). In this study, we found the lightning activity enhanced under polluted condition resulting from increasing ice crystal number and radius of graupel particles. More ice-phase particles existed at upper levels under polluted condition, forming a relatively strong charge region, which is also indicated by Zhao et al. (2015).

The impacts of aerosol on lightning were investigated acting as CCN, however, aerosol also tends to affect electrification and lightning discharge by acting as ice nuclei (IN) through microphysical processes (Tao et al., 2012; Fan et al., 2017). More sensitive experiments are still needed to discuss the influences of aerosol on lightning due to microphysical and thermodynamic processes, acting as IN.

Data availability

To request the data given in this study, please contact Dr. Dongxia Liu at the Institute of Atmospheric Physics, Chinese Academy of Sciences, via email (liudx@mail.iap.ac.cn).

Author contributions

MS, XQ designed the research ideas for this study. MS carried the study out and

prepared the paper. EM provided analysis ideas for the microphysics and electrification. DL, YY and AF edited the paper. Other co-authors participated in science discussions and article modification.

520

Competing interests

The authors declare that they have no conflict of interest.

Acknowledgment

Reference

Altaratz O, Kucienska B, Kostinski A B, et al. Global association of aerosol with flash
530   density of intense lightning[J]. Environmental Research Letters, 2017, 12(11).

Altaratz O, Koren I, Yair Y, et al. Lightning response to smoke from Amazonian fires[J]. Geophysical Research Letters, 2010, 37(7).

Bougeault P, Lacarrere P. Parameterization of orography-induced turbulence in a mesobeta--scale model[J]. Monthly weather review, 1989, 117(8): 1872-1890.

535   Brooks I M, Saunders C P R, Mitzeva R P, et al. The effect on thunderstorm charging of the rate of rime accretion by graupel[J]. Atmospheric Research, 1997, 43(3): 277-295.

Chaudhuri S, Middey A. Effect of meteorological parameters and environmental pollution on thunderstorm and lightning activity over an urban metropolis of
540   India[J]. Urban Climate, 2013, 3: 67-75.

Chen Z, Qie X, Yair Y, et al. Electrical evolution of a rapidly developing MCS during its vigorous vertical growth phase[J]. Atmospheric Research, 2020, 246: 105201.

Chen F, Dudhia J. Coupling an advanced land surface–hydrology model with the Penn

State–NCAR MM5 modeling system. Part I: Model implementation and sensitivity[J]. Monthly weather review, 2001, 129(4): 569-585.

Dendy, Jr J E. Two multigrid methods for three-dimensional problems with discontinuous and anisotropic coefficients[J]. SIAM journal on scientific and statistical computing, 1987, 8(5): 673-685.

Dudhia J. Numerical study of convection observed during the winter monsoon experiment using a mesoscale two-dimensional model[J]. Journal of Atmospheric Sciences, 1989, 46(20): 3077-3107.

Dwyer J R. A fundamental limit on electric fields in air[J]. Geophysical Research Letters, 2003, 30(20).

Dye J E, Knight C A, Toutenhoofd V, et al. The Mechanism of Precipitation Formation in Northeastern Colorado Cumulus III. Coordinated Microphysical and Radar Observations and Summary[J]. Journal of the Atmospheric Sciences, 1974, 31(8): 2152-2159.

Fan J, Rosenfeld D, Zhang Y, et al. Substantial convection and precipitation enhancements by ultrafine aerosol particles[J]. Science, 2018, 359(6374): 411-418.

Fan J, Leung L R, Rosenfeld D, et al. Effects of cloud condensation nuclei and ice nucleating particles on precipitation processes and supercooled liquid in mixed-phase orographic clouds[J]. Atmospheric Chemistry and Physics, 2017, 17(2).

Fan J, Zhang R, Li G, et al. Effects of aerosols and relative humidity on cumulus clouds[J]. Journal of Geophysical Research: Atmospheres, 2007, 112(D14).

Fierro A O, Mansell E R, Mac Gorman D R, et al. The implementation of an explicit charging and discharge lightning scheme within the WRF-ARW model: Benchmark simulations of a continental squall line, a tropical cyclone, and a winter storm[J]. Monthly Weather Review, 2013, 141(7): 2390-2415.

Guo J, Deng M, Lee S S, et al. Delaying precipitation and lightning by air pollution over the Pearl River Delta. Part I: Observational analyses[J]. Journal of Geophysical Research: Atmospheres, 2016, 121(11): 6472-6488.

Hobbs P V, Rangno A L. Ice Particle Concentrations in Clouds[J]. Journal of the Atmospheric Sciences, 1985, 42(23): 2523-2549.

Hu J, Rosenfeld D, Ryzhkov A, et al. Polarimetric radar convective cell tracking reveals
large sensitivity of cloud precipitation and electrification properties to CCN[J].
Journal of Geophysical Research: Atmospheres, 2019, 124(22): 12194-12205.

Jayaratne E R, Saunders C P R, Hallett J. Laboratory studies of the charging of soft-hail
during ice crystal interactions[J]. Quarterly Journal of the Royal Meteorological
Society, 1983, 109(461): 609-630.

Jiang M, Feng J, Sun R, et al. Potential influences of neglecting aerosol effects on the
NCEP GFS precipitation forecast[J]. Atmospheric Chemistry and Physics, 2017,
17(22):13967-13982.

Kar S K, Liou Y A, Ha K J. Aerosol effects on the enhancement of cloud-to-ground
lightning over major urban areas of South Korea[J]. Atmospheric Research, 2009,
92(1):0-87.

Khain A, Rosenfeld D, Pokrovsky A. Aerosol impact on the dynamics and
microphysics of deep convective clouds[J]. Quarterly Journal of the Royal
Meteorological Society: A journal of the atmospheric sciences, applied
meteorology and physical oceanography, 2005, 131(611): 2639-2663.

Khain A, Cohen N, Lynn B, et al. Possible Aerosol Effects on Lightning Activity and
Structure of Hurricanes[J]. Journal of the Atmospheric Sciences, 2008,
65(12):3652-3677.

Kumjian M R, Ryzhkov A V, Melnikov V M, et al. Rapid-scan super-resolution
observations of a cyclic supercell with a dual-polarization WSR-88D[J]. Monthly
weather review, 2010, 138(10): 3762-3786.

Liu D, Sun M, Su D, et al. A five-year climatological lightning characteristics of linear
mesoscale convective systems over North China[J]. Atmospheric Research, 2021,
256: 105580.

Li X, Zhang Q, Xue H. The role of initial cloud condensation nuclei concentration in
hail using the WRF NSSL 2-moment microphysics scheme[J]. Advances in
Atmospheric Sciences, 2017, 34(9): 1106-1120.

Liu Z, Gao W, Yu Y, et al. Characteristics of PM 2.5 mass concentrations and chemical
species in urban and background areas of China: emerging results from the CARE-

China network[J]. Atmospheric Chemistry and Physics, 2018, 18(12): 8849-8871.

605   Li Z, Wang Y, Guo J, et al. East asian study of tropospheric aerosols and their impact on regional clouds, precipitation, and climate (EAST‑AIRCPC)[J]. Journal of Geophysical Research: Atmospheres, 2019, 124(23): 13026-13054.

Lynn B, Yair Y, Shpund J, et al. Using Factor Separation to Elucidate the Respective Contributions of Desert Dust and Urban Pollution to the 4 January 2020 Tel Aviv

610   Lightning and Flash Flood Disaster[J]. Journal of Geophysical Research: Atmospheres, 2020, 125(24): e2020JD033520.

Lynn B, Khain A, Rosenfeld D, et al. Effects of aerosols on precipitation from orographic clouds[J]. Journal of Geophysical Research: Atmospheres, 2007, 112(D10).

615   MacGorman D R, Rust W D, Schuur T J, et al. TELEX the thunderstorm electrification and lightning experiment[J]. Bulletin of the American Meteorological Society, 2008, 89(7): 997-1014.

Mansell E R, Ziegler C L. Aerosol effects on simulated storm electrification and precipitation in a two-moment bulk microphysics model[J]. Journal of the

620   Atmospheric Sciences, 2013, 70(7): 2032-2050.

Mansell E R, Ziegler C L, Bruning E C. Simulated electrification of a small thunderstorm with two-moment bulk microphysics[J]. Journal of the Atmospheric Sciences, 2010, 67(1): 171-194.

Mansell E R, MacGorman D R, Ziegler C L, et al. Charge structure and lightning

625   sensitivity in a simulated multicell thunderstorm[J]. Journal of Geophysical Research: Atmospheres, 2005, 110(D12).

Mitzeva R, Latham J, Petrova S. A comparative modeling study of the early electrical development of maritime and continental thunderstorms[J]. Atmospheric research, 2006, 82(1-2): 26-36.

630   Mlawer E J, Taubman S J, Brown P D, et al. Radiative transfer for inhomogeneous atmospheres: RRTM, a validated correlated‑k model for the longwave[J]. Journal of Geophysical Research: Atmospheres, 1997, 102(D14): 16663-16682.

Naccarato K P, Pinto Jr O, Pinto I. Evidence of thermal and aerosol effects on the cloud-

to-ground lightning density and polarity over large urban areas of Southeastern Brazil[J]. Geophysical Research Letters, 2003, 30(13).

Orville R E, Huffines G, Nielsen‑Gammon J, et al. Enhancement of cloud-to-ground lightning over Houston, Texas[J]. Geophysical Research Letters, 2001, 28(13): 2597-2600.

Price C. Global surface temperatures and the atmospheric electrical circuit[J]. Geophysical Research Letters, 1993, 20(13): 1363-1366.

Price C, Rind D. A simple lightning parameterization for calculating global lightning distributions[J]. Journal of Geophysical Research Atmospheres, 1992, 97(D9):9919-9933.

Qie K, Qie X, Tian W. Increasing trend of lightning activity in the South Asia region[J]. Science Bulletin, 2021, 66(1): 78-84.

Qie X, Yuan S, Chen Z, et al. Understanding the dynamical-microphysical-electrical processes associated with severe thunderstorms over the Beijing metropolitan region[J]. Science China Earth Sciences, 2020: 1-17.

Qie X, Yuan T, Xie Y, et al. Spatial and temporal distribution of lightning activities on the Tibetan Plateau[J]. Chinese Journal of Geophysics, 2004, 47(6): 1122-1127.

Reynolds S E, Brook M, Gourley M F. Thunderstorm charge separation[J]. Journal of Meteorology, 1957, 14(5): 426-436.

Rosenfeld D, Lohmann U, Raga G B, et al. 2008. Flood or drought: How do aerosols affect precipitation?[J]. Science, 321(5894): 1309-1313.

Rosenfeld D, Woodley W L. 2000. Deep convective clouds with sustained supercooled liquid water down to -37.5 ℃[J]. Nature, 405(6785): 440.

Saunders C P R, Peck S L, Varela G G A, et al. A laboratory study of the influence of water vapour and mixing on the charge transfer process during collisions between ice crystals and graupel[J]. Atmospheric Research, 2001, 58(3):187-203.

Saunders C P R, Peck S L. Laboratory studies of the influence of the rime accretion rate on charge transfer during crystal/graupel collisions[J]. Journal of Geophysical Research: Atmospheres, 1998, 103(D12): 13949-13956.

Saunders C P R, Keith W D, Mitzeva R P. The effect of liquid water on thunderstorm

charging[J]. Journal of Geophysical Research: Atmospheres, 1991, 96(D6): 11007-11017.

Simpson G C, Scrase F J. The distribution of electricity in thunderclouds[J]. Proceedings of the Royal Society of London. Series A-Mathematical and Physical Sciences, 1937, 161(906): 309-352.

Srivastava A, Tian Y, Qie X S, et al. 2017. Performance assessment of Beijing Lightning Network (BLNET) and comparison with other lightning location networks across Beijing. Atmospheric Research, 197 76-83.

Stolz D C, Rutledge S A, Pierce J R. Simultaneous influences of thermodynamics and aerosols on deep convection and lightning in the tropics[J]. Journal of Geophysical Research: Atmospheres, 2015, 120(12): 6207-6231.

Storer R L, Van Den Heever S C, Stephens G L. Modeling aerosol impacts on convective storms in different environments[J]. Journal of the Atmospheric Sciences, 2010, 67(12): 3904-3915.

Sun M, Qie X, Liu D, et al. Analysis of potential effects of aerosol on lightning activity in Beijing metropolitan region[J]. Chinese Journal of Geophysics, 2020, 63(5): 1766-1774.

Takahashi T. A numerical simulation of winter cumulus electrification. Part I: Shallow cloud[J]. Journal of the Atmospheric Sciences, 1983, 40(5): 1257-1280.

Takahashi T. Riming electrification as a charge generation mechanism in thunderstorms[J]. Journal of the Atmospheric Sciences, 1978, 35(8): 1536-1548.

Tan Y B, Ma X, Xiang C Y, et al. A numerical study of the effects of aerosol on electrification and lightning discharges during thunderstorms[J]. Chinese Journal of Geophysics, 2017, 60(8): 3041-3050.

Tao W K, Chen J P, Li Z, et al. Impact of aerosols on convective clouds and precipitation[J]. Reviews of Geophysics, 2012, 50(2).

Thomas R J, Krehbiel P R, Rison W, et al. Observations of VHF source powers radiated by lightning[J]. Geophysical Research Letters, 2001, 28(1): 143-146.

Thornton J A, Virts K S, Holzworth R H, et al. 2017. Lightning enhancement over major oceanic shipping lanes[J]. Geophysical Research Letters, 44(17).

Twomey, S., 1959: The nuclei of natural cloud formation, Part II: The supersaturation in natural clouds and the variation of cloud droplet concentration. Geofis. Pura Appl., 43, 243–249.

Van Den Broeke M S, Straka J M, Rasmussen E N. Polarimetric radar observations at low levels during tornado life cycles in a small sample of classic southern plains supercells[J]. Journal of applied meteorology and climatology, 2008, 47(4): 1232-1247.

Wang Q, Li Z, Guo J, et al. 2018. The climate impact of aerosols on the lightning flash rate: is it detectable from long-term measurements?[J]. Atmospheric Chemistry and Physics, 18(17).

Wang Y, Qie X S, Wang D F, et al. 2016. Beijing Lightning Network (BLNET) and the observation on preliminary breakdown processes [J]. Atmos. Res., 171: 121–132.

Wang Y, Wan Q, Meng W, et al. Long-term impacts of aerosols on precipitation and lightning over the Pearl River Delta megacity area in China[J]. Atmospheric Chemistry and Physics, 2011, 11(23): 12421-12436.

Westcott N E. Summertime cloud-to-ground lightning activity around major Midwestern urban areas[J]. Journal of Applied Meteorology, 1995, 34(7): 1633-1642.

Williams E, Mushtak V, Rosenfeld D, et al. Thermodynamic conditions favorable to superlative thunderstorm updraft, mixed phase microphysics and lightning flash rate[J]. Atmospheric Research, 2005, 76(1-4): 288-306.

Williams E, Stanfill S. The physical origin of the land–ocean contrast in lightning activity[J]. Comptes Rendus Physique, 2002, 3(10): 1277-1292.

Williams E. The tripole structure of thunderstorms[J]. Journal of Geophysical Research, 1989: 13151-13167.

Xiong Y J, Qie X S, Zhou Y J, et al. Regional responses of lightning activities to relative humidity of the surface[J]. Chinese Journal of Geophysics, 2006, 49(2): 311-318.

Yair Y, Lynn B, Yaffe M, et al. Observations and numerical simulations of the October 25th, 2015 super-cell thunderstorm over Central Israel[J]. Atmospheric Research, 2021, 247: 105165.

Yair Y. Lightning hazards to human societies in a changing climate[J]. Environmental Research Letters, 2018, 13(12).

Yair Y, Lynn B, Price C, et al. Predicting the potential for lightning activity in Mediterranean storms based on the Weather Research and Forecasting (WRF) model dynamic and microphysical fields[J]. Journal of Geophysical Research, 2010.

Yair Y. Charge generation and separation processes[J]. Space Science Reviews, 2008, 137(1-4): 119-131.

Yuan T, Remer L A, Pickering K E, et al. Observational evidence of aerosol enhancement of lightning activity and convective invigoration[J]. Geophysical Research Letters, 2011, 38(4).

Zhang R, Jing J, Tao J, et al. Chemical characterization and source apportionment of PM 2.5 in Beijing: seasonal perspective[J]. Atmospheric Chemistry and Physics, 2013, 13(14): 7053-7074.

Zhao P, Li Z, Xiao H, et al. Distinct aerosol effects on cloud-to-ground lightning in the plateau and basin regions of Sichuan, Southwest China[J]. Atmospheric Chemistry and Physics, 2020, 20(21): 13379-13397.

Zhao P, Yin Y, Xiao H. The effects of aerosol on development of thunderstorm electrification: A numerical study[J]. Atmospheric Research, 2015, 153: 376-391.

Ziegler C L, MacGorman D R. Observed lightning morphology relative to modeled space charge and electric field distributions in a tornadic storm[J]. Journal of Atmospheric Sciences, 1994, 51(6): 833-851.

Ziegler C L, MacGorman D R, Dye J E, et al. A model evaluation of noninductive graupel‐ice charging in the early electrification of a mountain thunderstorm[J]. Journal of Geophysical Research: Atmospheres, 1991, 96(D7): 12833-12855.

Ziegler C L. Retrieval of thermal and microphysical variables in observed convective storms. Part 1: Model development and preliminary testing[J]. Journal of the Atmospheric Sciences, 1985, 42(14): 1487-1509.

Table 1. Settings for the nested simulations

Model Option	Outer D01	Inner D02
Domain Coverage	6 km, 442×391	2 km, 496×496
Vertical levels	40	40
Time step	30 s	10 s
Microphysics Scheme	NSSL two-moment	NSSL two-moment
Longwave Radiation	RRTM	RRTM
Shortwave Radiation	Dudhia	Dudhia
Boundary Layer	BouLac PBL	BouLac PBL
Land Surface	Unified Noah LSM	Unified Noah LSM

Table 2. Temporal evolution of the thunderstorm.

	Observation (UTC)	Simulations (UTC)	
		C-case	P-case
Formation	10:48	09:18	09:18
Beginning stage	10:48-11:30	09:18-09:30	09:18-10:00
Developing stage	11:30-12:30	09:30-10:30	10:00-11:00
Mature stage	12:30-13:30	10:30-12:00	11:00-12:36
Dissipating stage	13:30-18:06	12:00-15:36	12:36-16:36

Table 3. Domain-averaged Properties of Hydrometeors.

	Number Concentration (10^3 kg^{-1})		Mean-mass Radius (μm)	
	C-case	P-case	C-case	P-case
Cloud droplets	3930	7910	6.5	6.1
Rain drops	0.069	0.031	154.1	179.9
Ice Crystals	2280	3850	3235.8	2994.9
Graupel	0.028	0.012	322.4	479.5

Table 4. Comparison of Convective Properties.

765

	C-case	P-case
Time	10:36 UTC	10:48 UTC
Height	10.5 km	12.5 km
Maximum velocity	50.4 m/s	53.5 m/s
Cloud top height	15 km	15 km
Cloud base height	0.5 km	0.5 km
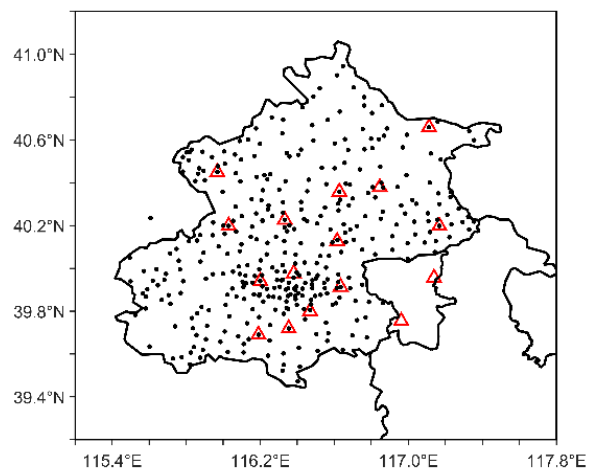
770   **Figure 1** Spatial distributions of BLNET stations (red triangles), and ground-based automatic weather stations (black dots) in the Beijing region.
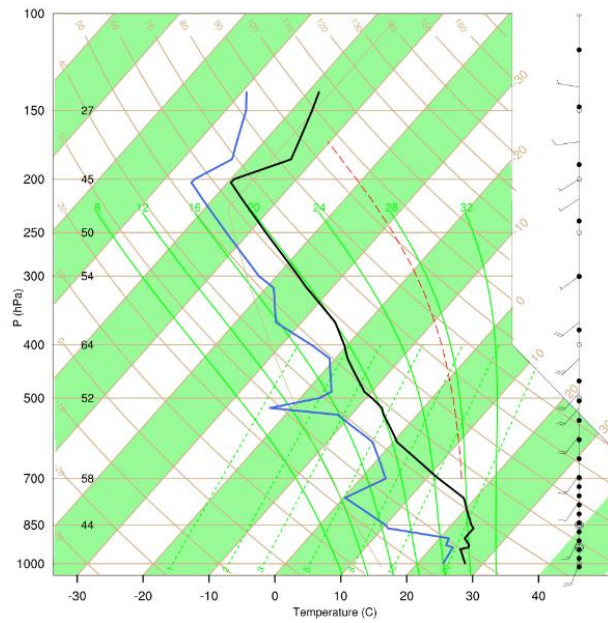
775   **Figure 2** Sounding profiles for Beijing at 00:00 UTC on Aug11, 2017. The black, blue solid lines and red dashed line represent temperature, dew point, parcel adiabatic lapse rate, respectively.
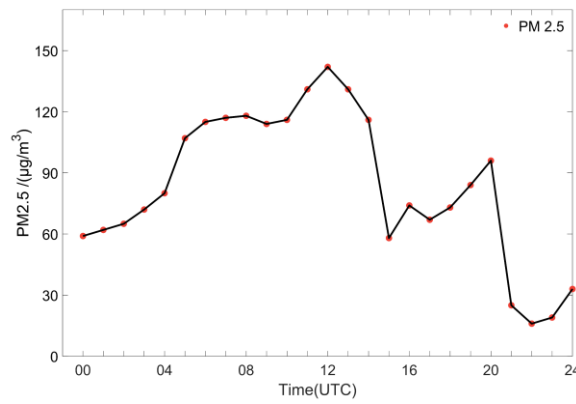
Figure 3 Hourly mass concentration of $PM_{2.5}$ on Aug11, 2017 at Beijing urban area.

780
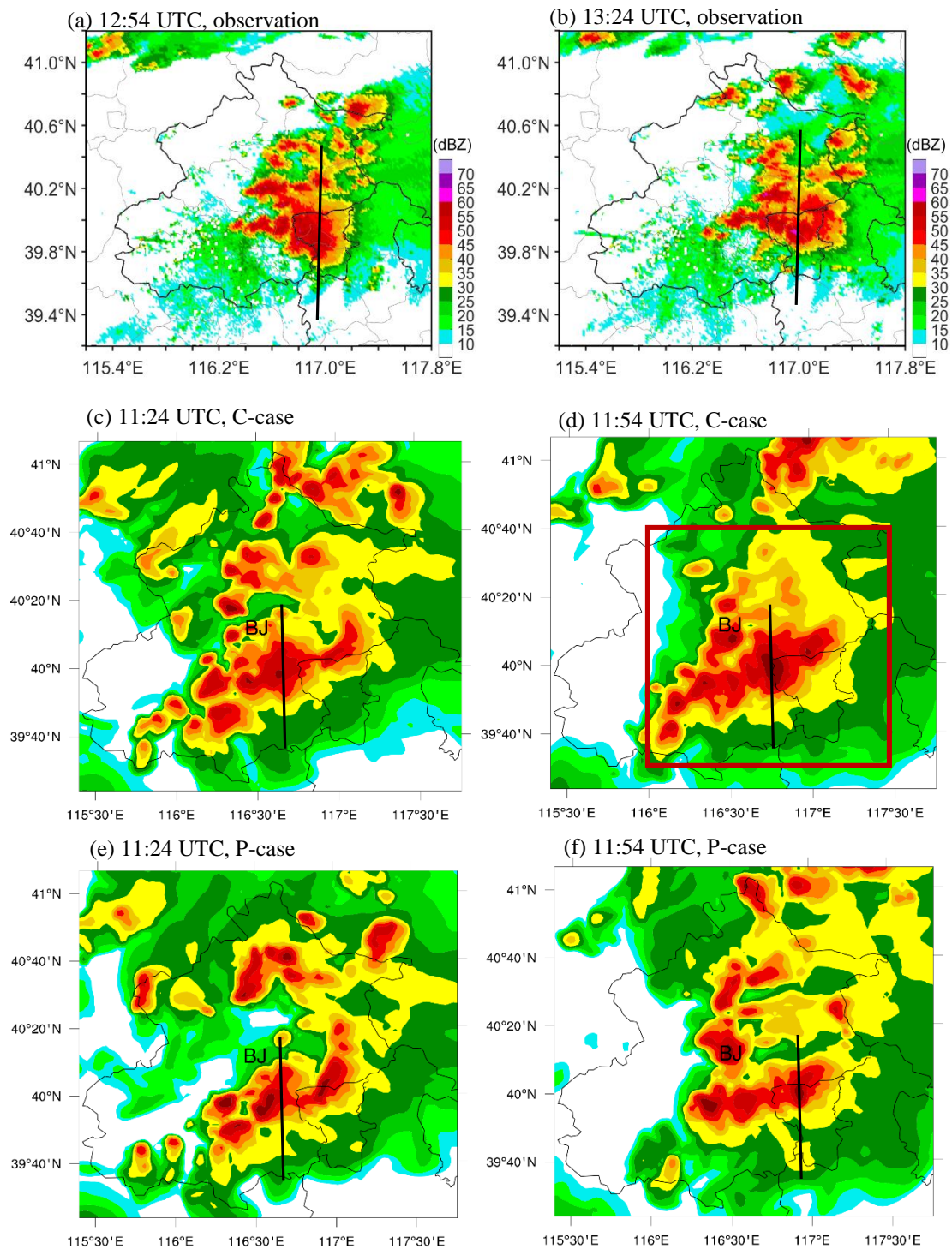
Figure 4 Radar reflectivity (unit: dBZ) between observation and simulation for the C- and P-cases, the simulation was earlier than observation about 1.5 h. (a)-(b) Observation at 12:54 UTC and 13:24 UTC. (c)-(d) Simulation for the C-case at 11:24 UTC and 11:54 UTC. (e)-(f) Simulation for the P-case at 11:24 UTC and 11:54 UTC, respectively. The red rectangle in Fig. 4d denotes the region where the simulated results are analyzed in this study.
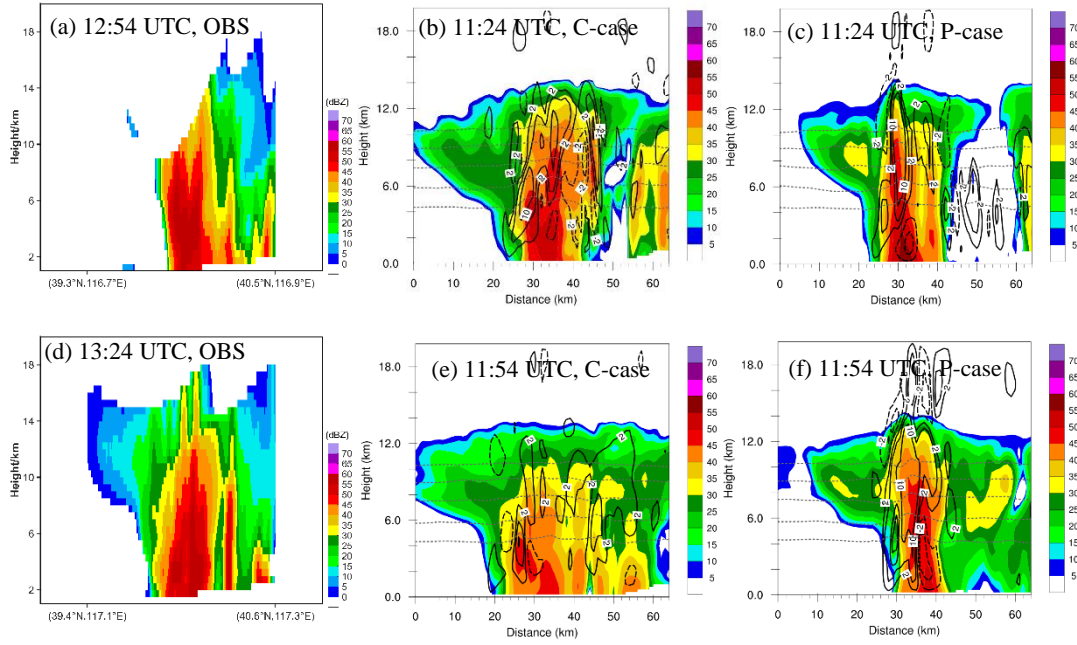
Figure 5 Comparison of vertical cross-section of radar reflectivity along the black line shown in Figure 4a-4f between observation and simulations. (a) Observation (black line shown in Fig.4a), (b) C-case (black line in Fig. 4c), (c) P-case (black line in Fig. 4e), (d) Observation (black line shown in Fig. 4b). (e) C-case (black line in Fig. 4d), and (f) P-case (black line in Fig. 4f).
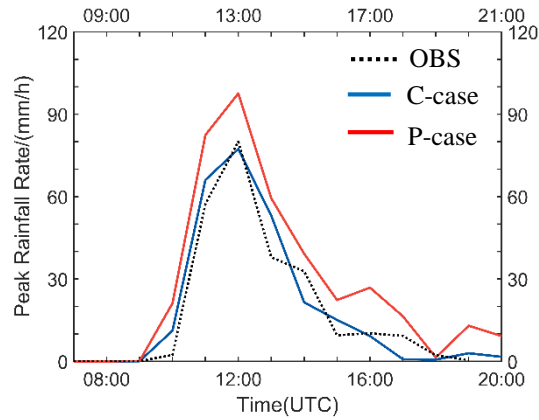
Figure 6 Temporal evolution of the peak rainfall rate for observation and simulations. The black dashed line represents the observation, the red line corresponds to the P-case, and the blue line corresponds to the C-case. The x-axis above is for the observation, the x-axis below is for the simulations.
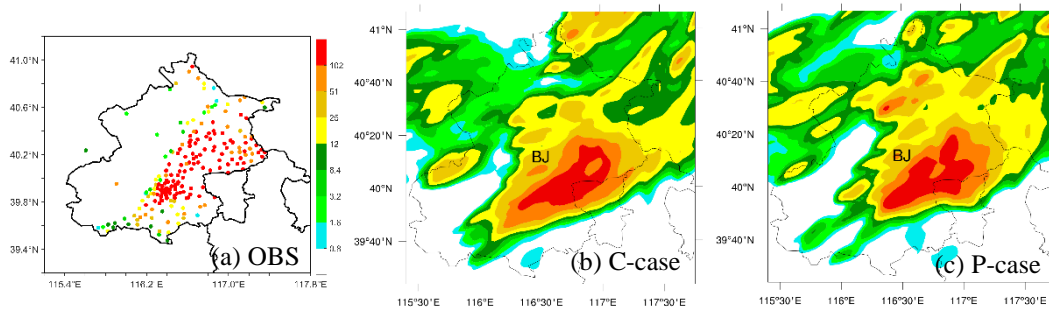
Figure 7 Comparison of accumulated precipitation (units: mm) between observation (11:00-17:00 UTC) and simulations (10:00-16:00 UTC). (a) Observation. (b) C-case, and (c) P-case.
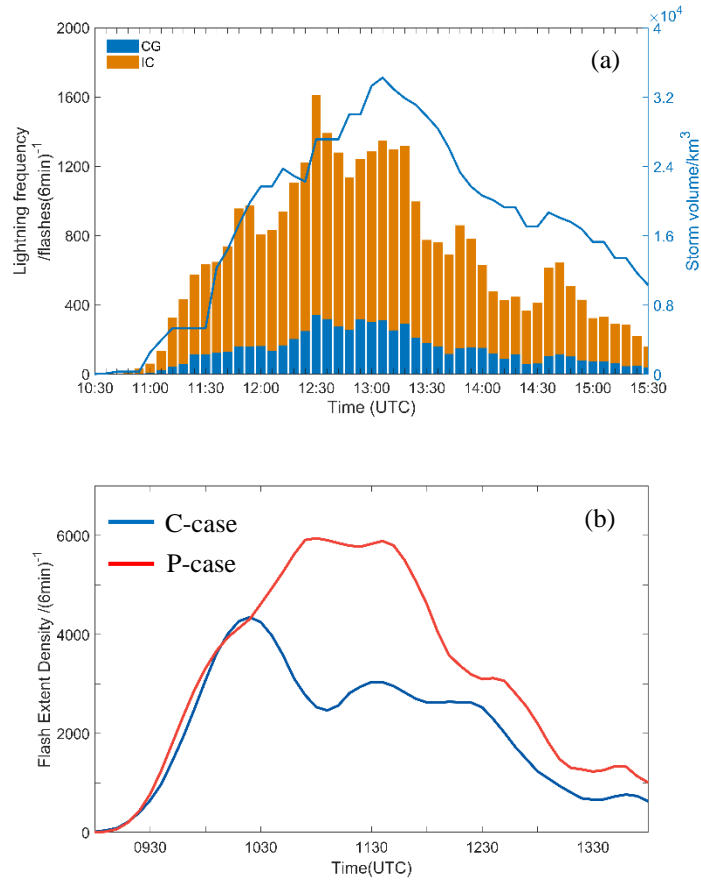
810 **Figure 8** Temporal variation in (a) observed total lightning frequency and (b) simulated flash extent density (FED). In (a), orange represents IC lightning and blue represents CG lightning. The solid line represents the storm volume associated with radar reflectivity exceeding 30 dBZ. In (b), red line represents the P-case and blue line represents the C-case.
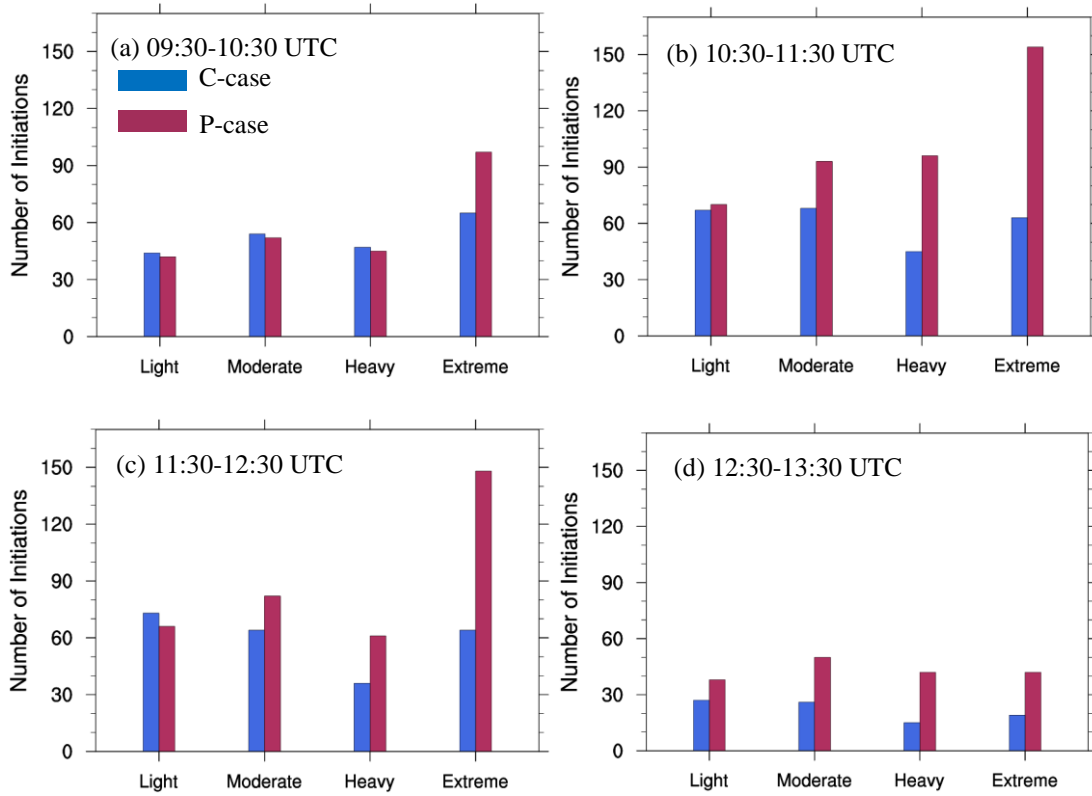
Figure 9 Number of initiations for different lightning intensity categories in different time, i.e. light (50-100 grid points), moderate (100-200 grid points), heavy (200-300 grid points) and extreme (>300 grid points), simulated for the P- and C-cases.

820

815

825
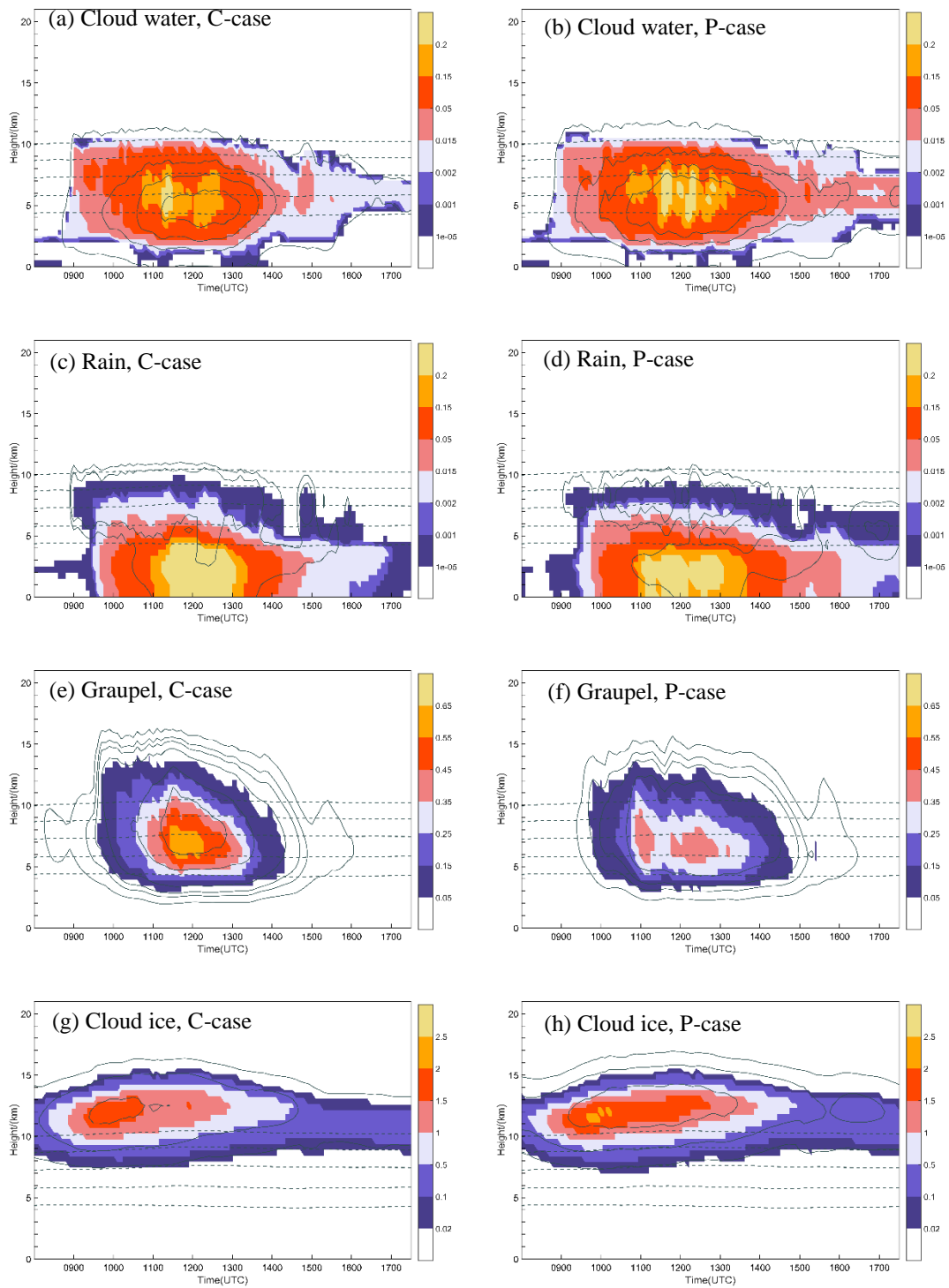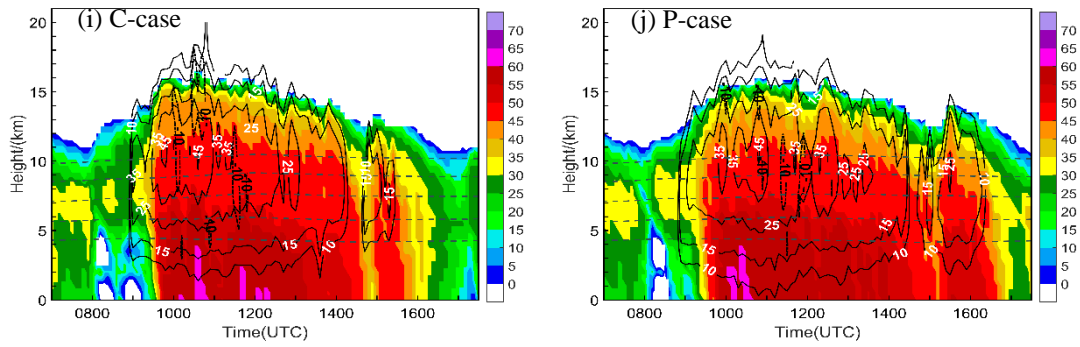
Figure 10 (a)-(h) Temporal variation of the vertical profiles of domain-averaged mass mixing ratio (g kg^{-1}, shaded) and number concentration (kg^{-1}, solid lines) of (a) cloud water in the C-case, (b) cloud water in P-case, (c) rain water in the C-case, (d) rain water in the P-case, (e) graupel in the C-case, (f) graupel in the P-case, (g) ice in the C-case, (h) ice in the P-case. Contour levels in (a)-(h) for cloud water number concentration are 10^6, 2×10^7, 5×10^7, 10^8 kg^{-1}, and for rain water are 100, 300 kg^{-1}, and for graupel are 10, 30, 50, 100, 300, 500, 700, 1000 kg^{-1}, and for ice are 0.1×10^7, 1×10^7, 5×10^7 kg^{-1}. (i)-(j) Time-height maximum simulated radar reflectivity (color shading, unit: dBZ) and maximum vertical velocities (solid line and white label: 10, 15, 25, 35, 45 m s^{-1}; dashed line and black label: -10, -15 m s^{-1}) for (i) the C-case and (j) the P-case. The 0 ℃, -10 ℃, -20 ℃, -30 ℃ and -40 ℃ isotherms are shown by the dashed gray lines in (a)-(j).
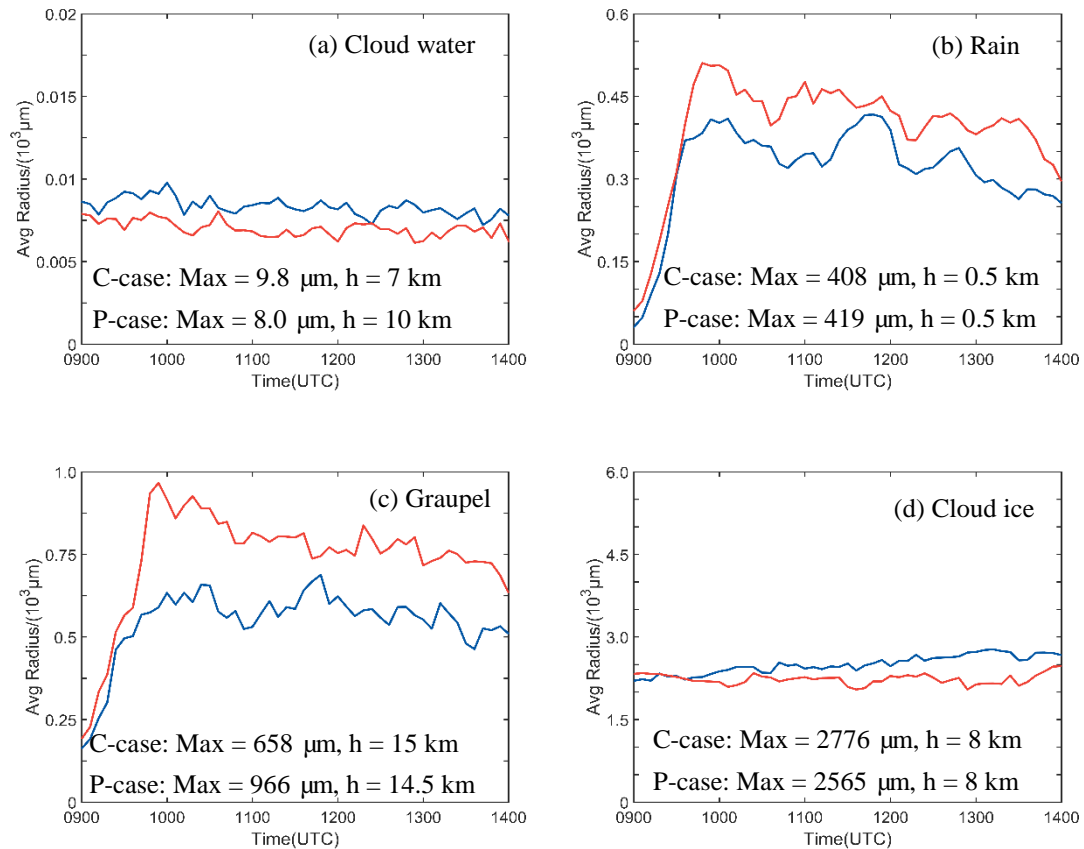
Figure 11 Temporal variation of domain-averaged effective radius for the different hydrometeors. (a) cloud water, (b) rainwater, (c) graupel, (d) ice. The red lines represent the P-case and the blue lines represent the C-case.
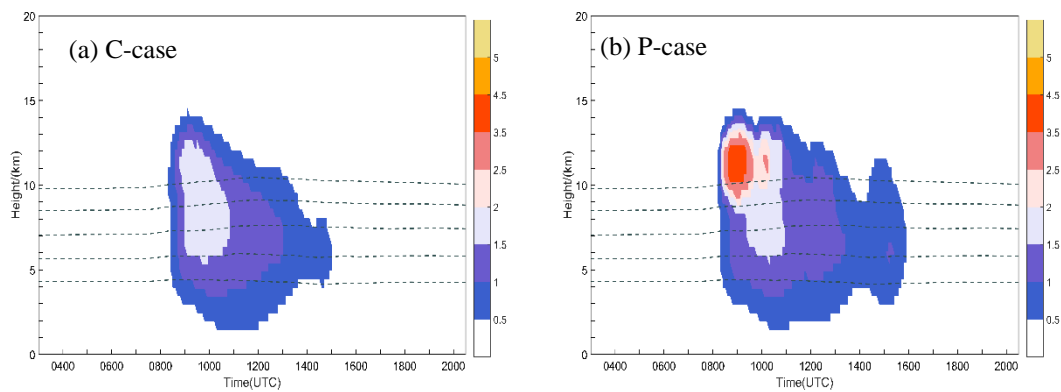

Figure 12 Temporal variation of the vertical profiles of peak latent heating (K hour^{-1}, shaded) of (a) C-case, and (b) P-case. The 0 ℃, -10 ℃, -20 ℃, -30 ℃ and -40 ℃ isotherms are shown by the dashed gray lines in (a)-(b).
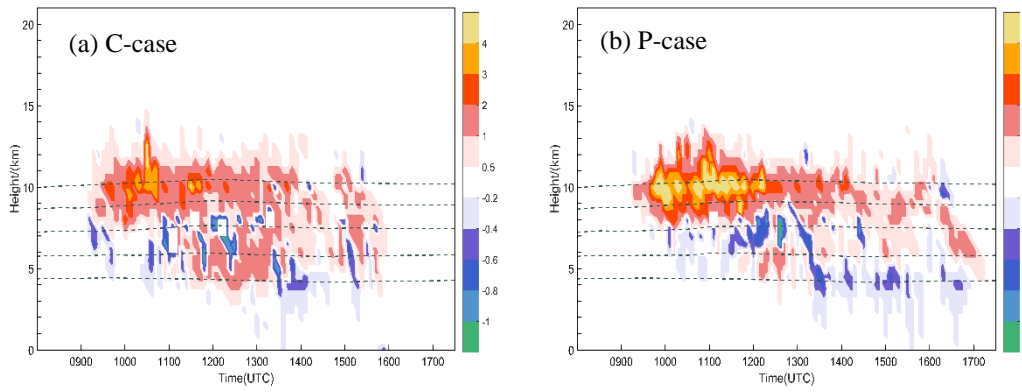
Figure 13 Temporal variation of the vertical profiles of peak positive (negative) charge density (nC m^{-3}, shaded) of (a) C-case, and (b) P-case. The 0 ℃, -10 ℃, -20 ℃, -30 ℃ and -40 ℃ isotherms are shown by the dashed gray lines in (a)-(b).
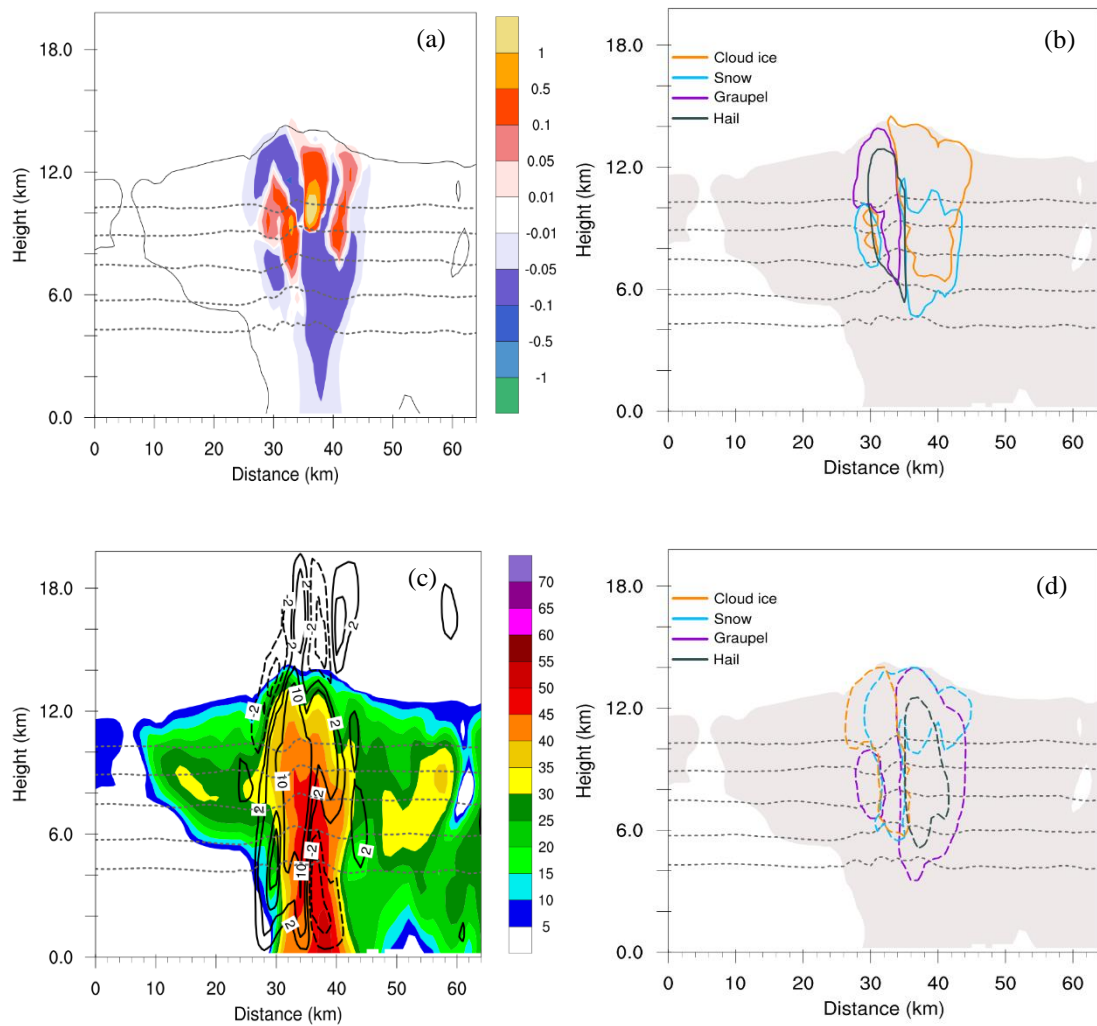
Figure 14 Vertical cross sections (south to north) at the location shown in Fig. 4f of simulated variables at the mature stage of the thunderstorm (11:54 UTC) in the P-case. (a) Total net space charge (nC m^{-3}, shaded). The 0 ℃, -10 ℃, -20 ℃, -30 ℃ and -40 ℃ isotherms are shown by dashed gray lines in (a)-(d). (b) +0.1 nC m^{-3} space charge density contours for cloud ice (orange), snow (blue), graupel (purple), and hail (black). The cloud outline (reflectivity echoes ≥ 5 dBZ) is denoted by the gray shaded contour. (c) Radar reflectivity (unit: dBZ), black lines for vertical velocities (solid line: 2, 5, 10 m s^{-1}; dashed line: -2 m s^{-1}). (d) As in (b), but for -0.1 nC m^{-3} charge density.
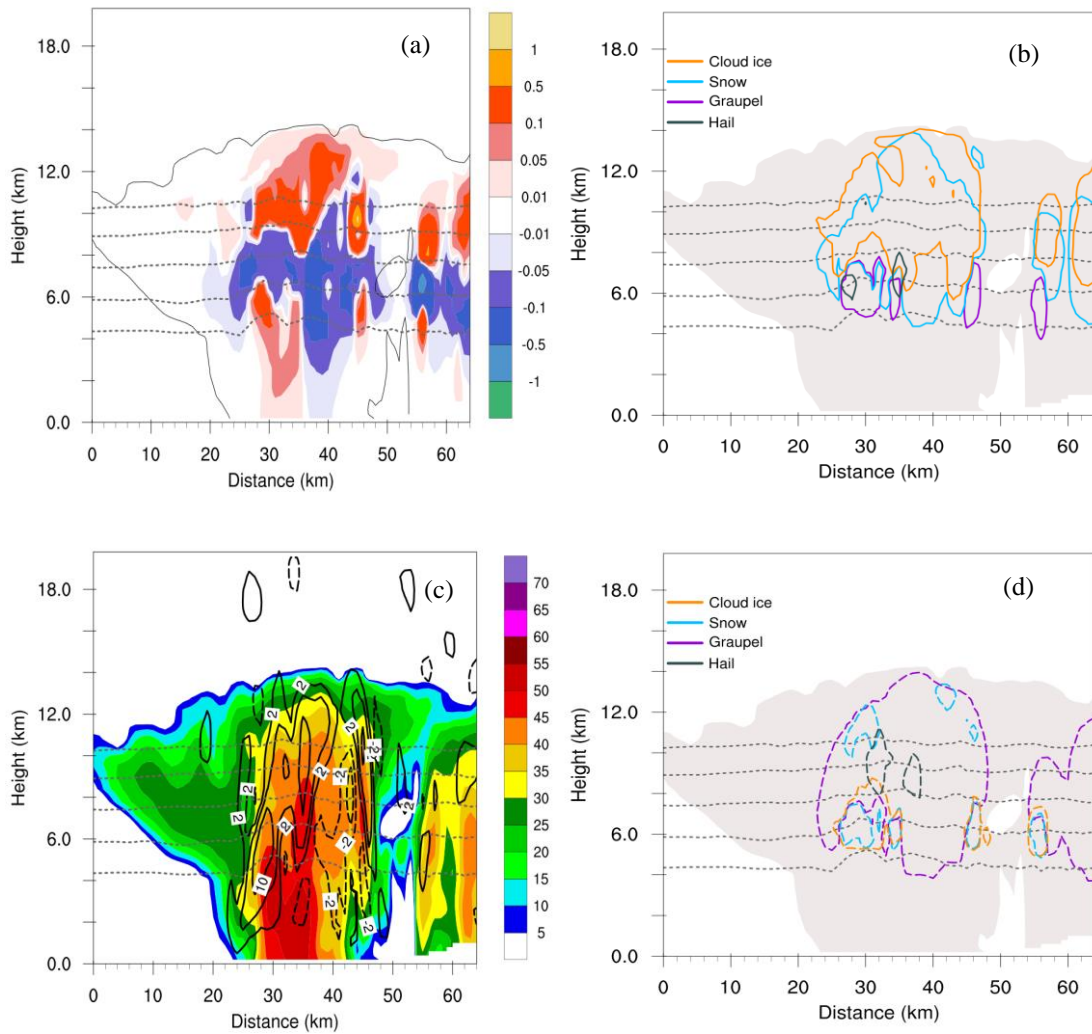
Figure 15 As in Fig. 14, but the vertical cross sections at the location shown in Fig. 4c of simulated
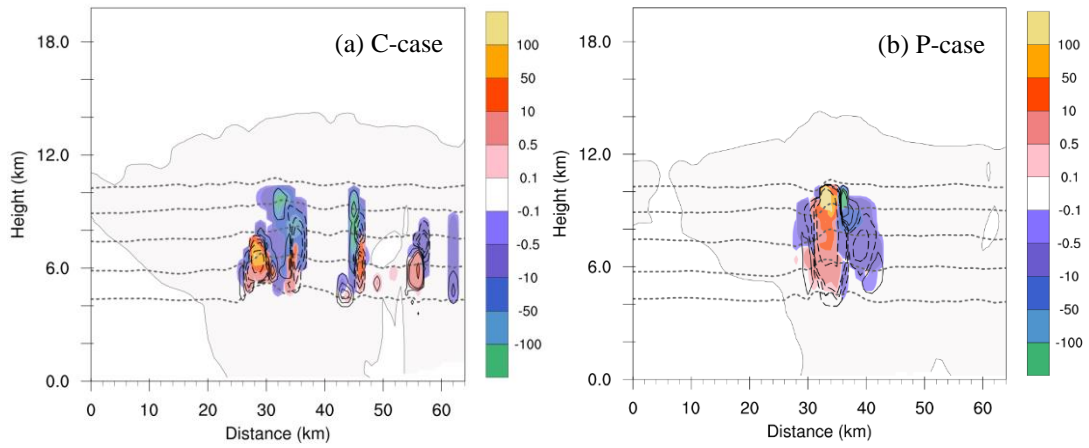variables at the mature stage of the thunderstorm (11:24 UTC) in the C-case.

Figure 16 Vertical cross sections (south to north) at the locations shown in Fig. 4c and 4f of non-inductive (pC m^{-3} s^{-1}, shaded) and inductive (solid lines: 0.1, 0.5, 1 pC m^{-3} s^{-1}; dashed lines: -0.1, -0.5, -1, -5, -10 pC m^{-3} s^{-1}) charging rates at the mature stage of (a) C-case (11:24 UTC, Fig. 4c), and (b) P-case (11:54 UTC, Fig. 4f). The 0 ℃, -10 ℃, -20 ℃, -30 ℃ and -40 ℃ isotherms are shown by dashed gray lines.